JOURNAL OF AIRCRAFT
Vol. 36, No. 3, May–June 1999

Investigation of Confluent Boundary Layers in High-Lift Flows

Susan X. Ying*
The Boeing Company, Long Beach, California 90807
Frank W. Spaid†
The Boeing Company, St. Louis, Missouri 63166
and
Catherine B. McGinley‡ and Christopher L. Rumsey§
NASA Langley Research Center, Hampton, Virginia 23681

The confluent boundary layers over a three-element high-lift airfoil are studied using both numerical and experimental approaches. The results suggest that wake prediction is crucial to the convergence and accuracy of the overall solution. At maximum lift, unsteadiness is observed in the experiment, which is not captured by computations. However, solutions at maximum lift indicate that, although the flow is attached over the flap, the separation bubble at the leading edge of the slat upper surface is coupled with inviscid flow reaching the compressibility limit. The thickened slat wake results in a displacement of near-surface flow over the main element and limits the main element from gaining more lift. The trends in the confluent boundary layers development require all aspects of the physics be modeled appropriately, including transition, turbulence, and inviscid–viscous interaction. An eddy viscosity turbulence model is shown to be ill-behaved for predicting some of the physics of wake confluence. Also, the isotropic eddy viscosity assumption is not strictly valid for the confluent boundary layers with large flow turning angles.

I. Introduction

IN the introduction of *Wing Design and Analysis—Your Job*, Smith[1] said ". . . the definition of an airplane . . . is a device that almost won't work." This statement characterizes the challenges of wing design, as the transport aircraft wing must be designed to operate in the entire flight envelope including cruise and low-speed conditions. Earlier airplanes did not require high-lift systems because their wing loadings were low and the speed ratios between cruise and low speed were also low. In contrast, modern commercial transport cruise speeds and wing loadings are much higher; consequently, a high-lift system is required to provide the additional lift necessary for low-speed operations. Moreover, the airfoil shapes and integrated wing planforms optimized for cruise performance impose challenging design constraints on the high-lift system. Nield[2] used an analogy of the childhood game of crack-the-whip to describe the process of the high-lift design development of the Boeing 777. He indicated that seemingly small changes to the wing to meet changing mission goals can totally invalidate the high-lift design for a preceding configuration. It follows that high-lift design must utilize rapid and efficient processes. This leads to the need for applying robust and reliable computational fluid dynamics (CFD) tools.

It has been two decades since Smith[3] presented his Wright Brothers Lecture on high-lift aerodynamics. Currently, CFD is still far from being an integral part of high-lift design process as it is in cruise wing design.[4] Even in two-dimensional high-lift flows, the computed trends still do not always agree with results of experiments. In particular, the pertinent flow features and physical effects attributed to configuration changes and flow conditions have not been consistently predicted by CFD.[5] To understand why CFD models do not adequately predict important flow features, and to improve prediction accuracy, it is imperative that we gain more insight into the physics governing high-lift flows. The difficulties confronting high-lift flow simulations lie primarily in the area of multiple viscous-layer interactions, or confluent boundary layers (CBLs). There have been many experimental investigations in the area of CBLs representative of high-lift flows (see references cited in Bucci and Sullivan[6] and Sec. II). However, very few of these experiments provide a complete set of detailed data, including transition and turbulence quantities at high Reynolds numbers for realistic high-lift configurations. In the spring of 1996, a workshop was held at the NASA Langley Research Center with McDonnell Douglas and Boeing participation to plan experiments to address critical high-lift flow physics issues pertaining to CFD development. The outcome was a coordinated effort between CFD and experimental investigators from NASA and Boeing to jointly study the transition and turbulence effects for the well-documented three-element high-lift airfoil considered in this study.

Based on the joint flow physics investigation, Rumsey et al.[7] recently reported the effect of varying the transition location and the use of a nonlinear explicit algebraic stress model for a representative high-lift wing section. The present paper expands on the work by Rumsey et al.[7] Our objective is to examine the detailed flowfield physics in an attempt to improve the CFD solution accuracy using both experimental flowfield surveys and Reynolds-averaged Navier–Stokes (RANS) simulations. In Sec. II, the physics pertinent to high-lift aerodynamics is reviewed. In Sec. III, both the experimental and CFD methods are introduced. Finally, in Sec. IV, measured mean velocities, Reynolds stress data, and numerical solutions are presented and discussed, including trends caused by flap gap variation and Reynolds number effects.

II. Review of High-Lift Flow Physics

A sketch of dominant flow features over a wing section in a high-lift configuration is illustrated in Fig. 1. The flowfield is characterized by significant interactions of the slat wake and wing, i.e., the main-element boundary layer (BL), and the CBL flow over the wing and flap surfaces. The BL from each element starts from the

Presented as Paper 98-2622 at the AIAA 16th Applied Aerodynamics Conference, Albuquerque, NM, June 15–18, 1998; received July 12, 1998; revision received Oct. 30, 1998; accepted for publication Nov. 2, 1998.

*Principal Engineer, Flight Performance, MC 078-0421. Associate Fellow AIAA.
†Manager, Experimental Fluid Dynamics, MC 106-7126. Associate Fellow AIAA.
‡Research Engineer, Fluid Mechanics and Acoustics Division, M/S 170. Senior Member AIAA.
§Research Scientist, Fluid Mechanics and Acoustics Division, M/S 128. Senior Member AIAA.

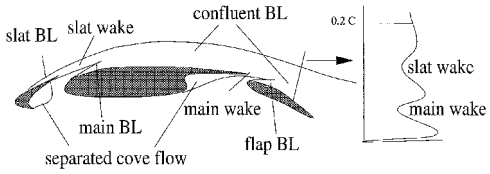

Fig. 1 Sketch of dominant physical features for high-lift flows.

attachment point near its leading edge (LE), and this fresh BL eventually merges with the wake shed by the previous element and a layer of unretarded air from the upstream gap. The CBL grows on the upper surface of the wing and flap, yielding a complex velocity profile that extends from the surface well into the flowfield, e.g., 20% chord above the flap surface at high incidence as shown. Because of the strongly coupled inviscid and viscous effects, this CBL can tolerate a much higher overall pressure rise without separation. Moreover, the wakes of the slat and main element can also penetrate regions of high adverse pressure gradient, making an efficient recovery off the surface. These important interactions between elements and between viscous and inertia forces have been summarized by Smith.[3] In three-dimensional configurations, the slats and flaps are typically only part-span, and they are supported by tracks and fairings. The presence of the fuselage and engine nacelles, in addition to the spanwise variation of slats and flaps, introduces more physical features into the high-lift problem, such as vortices trailing off the edges, junctions, and nacelle strakes. All of these geometric and physical factors make accurate prediction of high-lift characteristics a very challenging problem.

For a typical three-element airfoil at low incidence, the main element carries the highest loading, followed by the flap and slat. As the angle of attack increases, loading on both the main element and the slat increases. However, lift on the flap decreases, and the flap pressure suction peak becomes more moderate at high incidence. At stall, the main element reaches the maximum lift, while the flap continues to unload. In general, the BL on the flap with well-optimized gaps and overhangs is not separated at maximum lift.[8–10] For landing configurations, lift curves associated with this type of stall are relatively flat at maximum lift, indicating a gradual, gentle stall, unlike the LE-type stall often seen on single-element airfoils. If the combination of gaps and overhangs, or slat and flap deflections, are not set in optimum positions relative to each other, there can be flow separations on different elements at stall, as reviewed by Obert.[11]

The unique phenomenon of fully attached flow at stall has been observed on a Cessna L-19, as early as 1958 by Cornish.[12] Later it was shown by Petrov[13] that, although the flow was attached on the surfaces, the reduction in the rate of lift gain was associated with the appearance of a region of flow reversal, also noted as off-surface separation, situated in the wake off the flap surface. The flow reversal region was seen to grow thicker with increasing α and flap deflection. This phenomenon was said to limit the maximum obtainable lift. Petrov reports that the off-surface flow reversal region is quite stable. Nonetheless, several researchers investigating this flow in high-lift experiments with more realistic flow Reynolds numbers reported that there was no evidence of off-surface flow reversal,[14–16] although unsteadiness at maximum lift has been reported.[17] It is recognized that the displacement effect of the thick viscous layer leads to the large lift difference relative to the inviscid level at stall. Whether wake flow unsteadiness, off-surface flow reversal, some undiscovered physical behavior, or a combination of these factors is the lift-limiting mechanism, remains an open question today. Understanding this mechanism is important for implementing the correct physical modeling into CFD methods if we are to trust the maximum lift predictions.

Johnston and Horton[8] indicated that the development of high-lift viscous layers is affected significantly by flow curvature near stall conditions. They also found that for a two-element configuration there were significant static-pressure gradients normal to the surface, which invalidates methods using BL-type assumptions. Few experiments have been conducted to obtain measurements of mean flow and turbulence quantities to study the wake and BL interactions for realistic high-lift configurations. Brune and Sikavi[18] investigated the flowfield around a four-element airfoil in the Boeing Research Wind Tunnel. Their pitot probe and cross-wire probe measurements represent a self-consistent and sufficiently detailed database for CFD validation. However, the flow condition was at a chord Reynolds number (Re) of 1.55 million (M). Nakayama et al.[14] made detailed measurements of mean flow and turbulence quantities around a three-element airfoil at $Re = 3M$ in the NASA Langley Low Turbulence Pressure Tunnel (LTPT). They concluded that many parts of the shear flow deviate vastly from classical flows, including the strong curvature effects and significant static pressure variation normal to the airfoil surface. In subsequent tests at the LTPT tunnel, velocity profiles over the three-element airfoil used in this study have been taken to investigate the flowfield. It was found that the wake over the flap turned as much as 30–50 deg relative to the freestream.

Because of the complexity of the observed high-lift physics, there have been a number of building-block experiments aimed at gaining understanding by use of simplified models. Bario et al.[19] made measurements of a tandem symmetrical arrangement of a two-element airfoil in a variable-pressure gradient tunnel. They concluded that it was possible to separate the flow into three viscous regions: the wall BL, the internal half-wake, and the external half-wake. The laws of the wall and the wake provided valid descriptions of their observed velocity field, though the position of zero shear stress did not coincide with the position of zero velocity gradient. Zhou and Squire,[20] Agoropoulos and Squire,[21] and Squire[22] explored the interaction between the slat wake and the main-element BL. Squire also separated the wake and BL interaction into three successive regions, namely a) unmerged, with the wake and the BL separated by a potential core; b) initial merging of the viscous layers; and c) merged, where the velocity profile no longer features a wake. In particular, Squire indicated that there may be significant regions in the initial merging area, where the shear stress is of opposite sign to the velocity gradient. Sketches of the BL profiles corresponding to the three regions are shown in Fig. 2. For the high-lift configuration considered in this paper, the CBL over the main element contains a rapidly merging slat wake and main BL at low incidence, and the profile at midchord of the main element appears already fully merged. At high incidence, the slat wake merges later, and the profile over the flap surface still shows merging wakes. Even if transition was set according to experiment, the rapid merging of the slat wake and main BL still has not been predicted for low incidence by CFD.[7,23] Whether it is some unsteady flow off the slat trailing edge (TE), such as vortex shedding caused by slat cove flow, or another phenomenon such as a laminar bubble that was not modeled in the CFD, the reason for the disagreement between prediction and measurement is still not understood.

Using a simple two-element configuration, Johnston and Horton[8] adapted a multilayer representation of the merging viscous layers similar to that of Bario et al.[19] They also divided the viscous layers into three parts (Fig. 3): 1) the wall layer, from the surface to the first velocity maximum above surface (denoted by y_d); 2) the inner half-wake, from the wall layer boundary edge to the maximum velocity

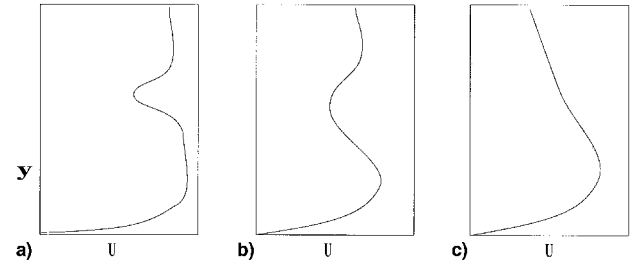

Fig. 2 Three regions of wake and BL interaction according to Squire[22]: a) unmerged, b) merging, and c) merged.

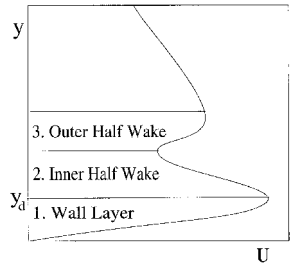

Fig. 3 Three parts of the confluent BL.[8]

deficit point in the wake; and 3) the outer half-wake, from the outer boundary of the inner half-wake to the edge of inviscid flow. By showing that the distance from the wall to the zero shear-stress point is less than y_d, they concluded that there is a small region at the vicinity of the wall layer and inner half-wake intersection where Reynolds shear stress ($-u'v'$) and normal velocity gradient ($\partial U/\partial y$) have opposite signs, in violation of the eddy viscosity (or Boussinesq) hypothesis. This situation is similar to the conclusion from Bario et al.[19] and those discovered from investigating curved mixing layers in Hinze[24] and Mathieu.[25]

There are several explanations for the non-Boussinesq-typephenomenon. Hinze argues that the turbulent transport cannot be of the gradient type only. Rather, in addition to the $\partial U/\partial y$ term, there is a contribution of larger-scale turbulence or of momentum transport over distances where the mean velocity gradient can no longer be considered as being constant, while the effect of turbulence inhomogeneity is felt. Mathieu pointed out the physical unreality of concepts such as those of Boussinesq and Prandtl. He also suggested that this phenomenon could be a result of the memory of the turbulent structures and of the effects of the transport phenomena. These explanations seem consistent with each other because small turbulent structures are not likely to yield the memory effect because they are rapidly suppressed by viscosity. Bario et al.[19] indicated that, because of the memory effect, such a structure conserves its identity for a certain distance after it penetrates the region of the inner half-wake, transporting with it the turbulent properties generated in the region of the outer wake. Consequently, in a limited region of the inner half-wake, and in spite of the negative velocity gradient, the total shear stress ($-u'v'$) remains positive.

A separate, yet important related issue to the Reynolds shear-stress measurement and interpretation is the use of an appropriate coordinate system. Traditionally, Reynolds stresses have been compared in BL coordinates, in which the mean and fluctuating velocity vectors are resolved in components normal and parallel to the surface. Johnson et al.[26] illustrated the difference of coordinate system orientation for Reynolds stress comparison over a NACA 4412 airfoil near the $C_{L_{\max}}$ condition. The two coordinate systems compared were the shear-layer aligned system (coordinates in which the flow direction is aligned to $U/U_e = 0.5$) and BL coordinates. They attributed the large differences in measured Reynolds stresses for the two different coordinate systems to 1) the flow in the separated BL being far from parallel with the surface and 2) the normal stress differences being large compared with the shear stresses. Unlike Johnson's example, for the baseline configuration and flow condition in this work, there is no separation over the flap surface. Nonetheless, the flow in the CBL becomes considerably less parallel to the surface away from the wall. As seen in the sketch of the high-lift CBL (Fig. 1), the thick viscous layer extends well into the flowfield. The local flow direction in the outer part of the layer can differ by more than 30 deg from that of the surface slope over the flap. Hence, for discussions of the CBL over the flap, we adopt the approach of using the streamline (SL) coordinate. This coordinate is similar to that of the shear-layer aligned system. However, unlike Johnson's approach of taking the flow direction at $U/U_e = 0.5$, in the SL coordinate the $u'v'$ at each point is rotated to the local flow direction. From the coordinate transformation relationship:

$$-u'v'|_\theta = -u'v'\cos(2\theta) + 0.5(u'u' - v'v')\sin(2\theta) \qquad (1)$$

where θ is the angle of rotation; the $u'v'$ in SL coordinates is obtained by substituting θ, calculated as the difference between the local flow angle and the measurement coordinate (BL) angle. It is evident that if θ is not negligible and/or the difference of normal stresses is large, then the shear stress at θ can be quite different from that evaluated in the local surface coordinates.

As seen from the preceding building-block-type studies, the physics of wake and BL interaction is very intricate and complex, even for one freestream flow condition, such as a fixed freestream Mach number and Reynolds number. There has been much work dedicated to understanding variations in high-lift flows caused by different freestream conditions, or scale effects. The results have been meticulously documented in the review paper by Haines.[27] In particular, the scale effect on $C_{L_{\max}}$ at high Reynolds number has become a very important topic, particularly since the discovery of adverse Reynolds number effects.[28–30] A remarkable analogy of the reverse Reynolds number effect on a transport wing with a highly deflected flap and the flap position effect over a quasi-two-dimensional single-slotted flap airfoil model has been demonstrated by Woodward et al.[31] They found that if the gap is fixed at the optimum for low Reynolds number, then raising the Reynolds number reduces the thickness of the BLs and the effective gap increases. This then can cause the peak suction on the aft element to rise and provoke a separation near the TE of the element, overriding the favorable effect of increasing Reynolds number on separation characteristics. This type of scale effect is of major concern to industry; because a high-lift configuration that performs well in a wind-tunnel environment at smaller scale, could perform poorly in a real flight condition at full scale. Clearly, we must obtain better understanding of the mechanisms that govern this scale effect, so that we can reliably simulate high-lift flows at actual flight conditions.

III. Methods

A. Experimental Approach

The high-lift airfoil geometry and flowfield measurement locations are depicted in Fig. 4. The streamwise coordinates in percent chord corresponding to these locations are also given in both stowed and unstowed coordinates. In this work, all streamwise location references will be made using the unstowed coordinates to avoid confusion. Velocity profiles have been obtained in three wind-tunnel entries, and Reynolds stresses have been obtained in two separate entries. A portion of the experimental results presented here were reported by Spaid and Lynch[16] and Chin et al.[17] Descriptions of the experimental apparatus and procedures are presented in those publications. These data were obtained with a multielement airfoil in the LTPT. Data obtained from these investigations consisted of surface static-pressure distributions and time-mean flowfield surveys with five-hole and flat-tube probes above the upper surfaces of the main element and the TE flap. Data from the flat-tube probe were used only for the portions of the profiles near the surface. Total-pressure measurements obtained with the flat-tube probe were corrected using data obtained from the five-hole probe during the same survey. The correction applied to the flat-tube probe data was assumed to be proportional to the local total pressure. Results were obtained at a Mach number of 0.2 and Reynolds numbers based on the clean (stowed) airfoil chord (c) of 5–16 M. The data include angles of attack beyond maximum lift.

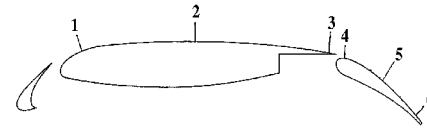

location	1	2	3	4	5	6
stowed	10.8	45	85	71.75	87.0	97.5
unstowed	10.8	45	85	89.82	103.2	111.2

Fig. 4 Experimental survey locations in percent chord.

In this paper, new results are presented in which fluctuating flowfield quantities were measured with a cross-wire probe. The traversing unit used in the previous investigations was modified to permit side-by-side mounting of a five-hole probe and a cross-wire probe. Each hot-wire sensor was 5 μm in diameter and had an unplated length of 1 mm. Calibrations were performed with the cross-wire probe mounted in the tunnel test section, with the sensing elements immersed in the potential core of a calibration jet. The tunnel circuit was pressurized to the test-section static pressure intended for the subsequent run. Several calibrations were performed at jet velocities that included the range of velocities anticipated for the subsequent run. At each jet velocity, the calibration jet nozzle and plenum were rotated in the pitch plane through ± 35 deg. Using an approach similiar to that of Lueptow et al.,[32] the calibration data were interpolated to form a regular grid and a two-dimensional polynomial was fitted to the data. The order of the polynomial was optimized to provide the best fit for each calibration. The procedure usually called for second- or third-degree polynomials. The average accuracy of the fit was 1.7% for angle and 0.5% for velocity. The temperature drift during a calibration or a survey run typically did not exceed 1°C. The temperature change between the time the calibration was performed and when the survey was taken averaged 5°C. The overheat ratio for the hot wires was maintained between the calibration and the survey runs. For the Reynolds stress surveys, data were sampled at 50 kHz and bandpass-filtered between 20 kHz and 20 Hz. During a run, the data were continuously sampled for 2 s at each point in a survey profile. Further details regarding the Reynolds stress measurement can be found in McGinley et al.[33]

B. CFD Method

The compressible, thin-layer RANS equations with a finite volume formulation are solved using the code CFL3D.[34–37] This code is globally second-order accurate in space. Upwind-biased spatial differencing is used for the inviscid terms, and flux limiting is used to obtain smooth solutions in the vicinity of shock waves, when present. Viscous terms are centrally differenced. The flux-difference-splitting scheme of Roe[38] is employed to obtain fluxes at the cell faces. The time-marching method is implicit, three-factor, approximate factorization. The implicit derivatives are written as spatially first-order accurate, which results in block-tridiagonal inversions for each sweep. However, for solutions that utilize Roe's scheme, the block-tridiagonal inversions are further simplified with a diagonal algorithm (with a spectral radius scaling of the viscous terms). The CFL3D code has been used successfully to compute multielement airfoil flowfields.[7,39,40] In addition to test run CFL3D with thin-layer assumption in both directions, independent computations[41] have also explored the effect of including the full Navier–Stokes terms for these flows on identical grids. It is concluded that the differences (including velocity profiles and turbulence quantities) are negligible compared with the thin-layer solutions presented here.

For simulating the flow around the high-lift configuration shown in Fig. 4, multiple-zone grids connected in a one-to-one matching manner were used.[7] Free-air outer boundary condition is used unless otherwise specified. The grid topology was chosen to best resolve the CBL physics and to ensure conservation across grid boundaries. Grid sequencing, multigrid, and local time stepping have been employed to accelerate convergence to steady state. Analyses of grid density effects have been performed in the previously mentioned references. Additionally, wind-tunnel wall effects and free-air outer boundary-condition effects have been documented[7] for the high-lift configuration studied here. In this work, the grid is also perturbed by adapting the original grid such that it is closely aligned to computed flow streamlines. Additionally, local grid refinement near the main-element trailing edge (MTE) is also tried. The Spalart–Allmaras[42] (S–A) one-equation eddy viscosity turbulence model is employed. For simulations involving transition to turbulence, the transition locations are specified using an approach similar to that taken by Rumsey et al.[7] using measurements from Bertelrud.[43]

IV. Results and Discussion

A. Flow Steadiness and Maximum Lift: CFD Convergence and Experimental Observations

The RANS equations are derived by averaging the viscous conservation laws over a time interval chosen large enough with respect to the time scale of the turbulent fluctuations. However, this time interval must also remain small with respect to the time scales of other time-dependent effects. Only when this is possible, the time-dependent Reynolds-averaged continuity equation remains unchanged for the mean quantities, and all of the effects of the turbulence on the averaged momentum conservation are contained in the Reynolds stress. As reviewed in Sec. II, and also discussed in Sec. IV.A.1, at near maximum lift ($C_{L_{\max}}$) conditions, the flow can be very unsteady. It is not clear yet whether this unsteadiness can be modeled by the RANS approach because the time scale has not been well documented.

1. *Convergence*

For the baseline configuration (Fig. 4), we examine the flow at $\alpha = 19$ deg and at maximum lift ($C_{L_{\max}}$), $\alpha = 21$ deg for $Re = 9M$, and freestream Mach number $M_{\text{fs}} = 0.2$. A normalized convergence history plot for $\alpha = 19$ deg is shown in Fig. 5, where the % Delta represents percentage difference with respect to the final converged result. At 5100 iterations, the solution converges to an L2-norm of the density residual of -9.3, representing a total drop of five orders of magnitude from the initial freestream condition. For the purposes of this illustration, we refer to this as the final converged result. An important observation is that inviscid properties such as pressure and total lift converge very rapidly compared with viscous properties. As C_L reaches 3% from its final value (C_{Lf}) at 2600 steps, or half of the total convergence time, C_D is still 20% from its final converged value (C_{Df}). It should be noted that, although the solution has not completely converged to machine accuracy after 5100 iterations, computations were also run out to 7600 iterations with density residual further decreased to -9.4, and less than an additional 0.2% change in lift, 0.9% in drag, and no appreciable change in the resulting velocity profiles.

Snapshots of a BL profile at $x/c = 0.45$ (location 2 in Fig. 4) at 2600 and 5100 steps (half vs full convergence) are presented in Fig. 6a. The corresponding turbulence profiles are also given in Fig. 6b. While the difference shown between these two convergence levels is subtle, it is clear that the biggest change in the profile from half convergence to full convergence is in the wake (due to the slat). This has two important implications: 1) when comparing the CFD viscous profiles with measurements, one must be sure to use a fully converged solution; 2) acceleration schemes for CFD flow solvers must take into account the wake convergence.

In Fig. 5, it is interesting to note that the convergence rate of the turbulence residual is almost identical to that of the drag. To investigate whether the turbulence model is the root cause of the slow convergence, we performed a simple test by restarting from

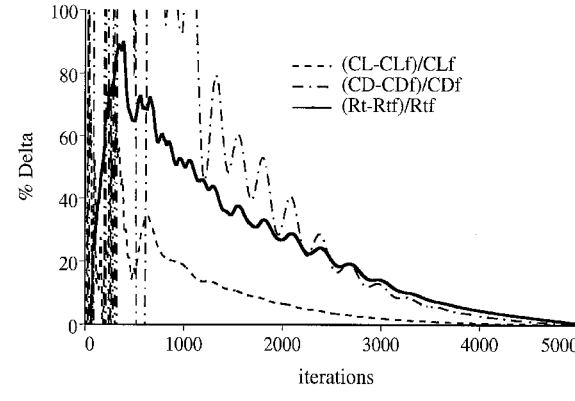

Fig. 5 Normalized convergence history.

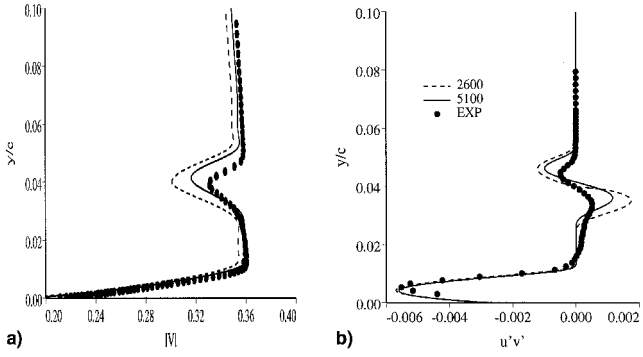

Fig. 6 a) Velocity profile comparison at *x/c* = 0.45 and b) Reynolds shear-stress comparison.

the solution at half convergence (or 2600 steps) and freezing the eddy viscosity. The final resulting convergence is just as slow as before, and the solution including the predicted Reynolds stress profile (not shown here) is also nearly the same as before. It appears that the turbulence model is not the cause of the slow convergence. The turbulence field seems to be effectively established within the first half of the convergence interval, after which the changes are minimal, i.e., not enough to make a significant impact on the mean-flow quantities. Hence, given half-converged wake-like eddy viscosity levels, the question arises as to why the wake mean flow is slow to converge. Is it a result of having BL-like high-aspect-ratio cells in the wake; although the wake grids are spread out downstream (in the direction normal to wake centerline) with lower aspect-ratio cells in general, perhaps the spreading rate is not fast enough? When the eddy viscosity is frozen, there is only the mean flow that is trying to react to the turbulence. Is the slow convergence a result of the separated cove flows, where small changes in pressure only slightly affect the lift, but rather result in large changes in drag, hence, the slow drag convergence and downstream wake convergence? In consideration of these open questions, future efforts to uncover and attempts to remove the root cause of this slow convergence seem prudent.

In Fig. 6b, the Reynolds stresses are in a fixed coordinate system aligned with the local surface normal (also referred to as BL coordinates), because the flow direction is almost aligned with the airfoil surface at this location. It should be noted that, because only the Reynolds shear stress is compared, the term Reynolds stress and the term $u'v'$ are both used loosely here and throughout the paper to refer to the Reynolds shear stress $u'_n v'_n$, where u'_n and v'_n are fluctuating components of the velocity in the local coordinate system chosen. Also note that in Fig. 6 and all subsequent profile plots, y/c refers to the local wall-normal distance nondimensionalized by the stowed airfoil chord. All velocity profiles presented are velocity magnitudes nondimensionalized by freestream speed of sound. All Reynolds stresses presented are nondimensionalized by the freestream velocity squared. Ignoring the slat wake, which is not accurately predicted by CFD, it can be seen that the Boussinesq assumption still appears valid at this midchord location within the main-element BL. Additionally, the CFD profiles (both mean and turbulent quantities) indicate that this is an unmerged region of the CBL (also see Fig. 2), i.e., there is a potential core between y/c of 0.01 and 0.03. However, the measured profiles suggest that the inner part of the slat wake and the main-element BL are already merging. This implies that CFD does not predict the same merging rate as observed in experiment. For lower angles of attack, the merging of the slat wake and main-element BL occurs even earlier; comparisons of mean velocity profiles at the same location are presented in Rumsey et al.[7]

2. *Maximum Lift*

At maximum lift ($\alpha = 21$ deg), experimental data indicate unsteadiness in the wake regions at stations near the flap TE. However, there is no flow separation on the main element or the flap

Table 1 Lift coefficients and maximum Mach for α = 19–24 deg

α	Slat	Main	Flap	Total	$M_{\max}$
19	0.7852	3.2758	0.3704	4.4315	1.0137
20	0.8344	3.3025	0.3550	4.4918	1.0966
21	0.8873	3.3337	0.3413	4.5624	1.2074
22	0.9381	3.3490	0.3268	4.6139	1.3477
23	0.9861	3.3454	0.3128	4.6444	1.4576
24	1.0245	3.2958	0.2968	4.6165	1.5092

for $\alpha = 21$ and 22 deg. Mean velocity profiles obtained from the five-hole probe at these aft locations show noticeably more scatter than at the forward stations. Furthermore, at the two stations near the TE ($x/c = 1.0321$ and 1.1125), there is a substantial increase in wake turbulence levels measured by the hot-wire probe.[33] It is possible that interference effects of the traversing unit contribute to the observed unsteadiness.

For the steady-state simulation with local time-stepping at $\alpha = 21$ deg, the initial solution convergence is similar to that of the $\alpha = 19$ deg case up to 5000 steps. However, there are small oscillations in drag, and eventually the amplitude grows. We terminated the steady run when the drag oscillation was beyond 10 counts. When the simulation is run with a second-order time-accurate scheme, the solution eventually settles to a steady state. Over 5.4 chord lengths were traveled in the interval of time-accurate simulation. We conclude that the oscillations seen in the steady-state simulation do not represent the true numerical solution, because using a uniform time step and the time-accurate scheme does not reproduce a similar unsteady phenomenon. The remaining question is: why does this peculiar phenomenon in the convergence of numerics happen at $\alpha = 21$ deg, the stalling angle observed in the experiment? To attempt to answer this question, we examine the solutions at all angles around $\alpha = 21$ deg and beyond the stall predicted by CFD for $Re = 9M$, and $M_{\text{fs}} = 0.2$.

The lift coefficients and maximum Mach number from the CFD solutions for $\alpha = 19$–24 deg are summarized in Table 1. Transition locations are specified for each case, although experimental transition data are only available up to 22 deg. At 22 deg, the transition region is slightly larger than that of 21 deg. However, in CFL3D only a point location can be specified to mark the extent (boundary) of the laminar region because the actual process of transition is not modeled. Transition over the slat LE is specified to be as close to the 21-deg case as possible, whereas the flow is kept attached without laminar separation, which can be numerically unstable. In particular, the transition location (endpoint) for the 22-deg solution is specified at 0.2% ahead of that for 21 deg. Similarly, for the solutions at 23 and 24 deg, the end of laminar region on the slat is fixed at the LE, which is 0.1% ahead of that for 22 deg. The solution convergence beyond $\alpha = 21$ deg is similar to that for $\alpha = 21$ deg, though for each case steady-state solution can be obtained using the time-accurate approach. The maximum lift is predicted at $\alpha = 23$ deg, which is 1 deg after the main element has reached its maximum lift. Detailed examination of the flow solutions indicates that there is no upper-surface separation on either the flap or the main element at stall. However, the flows around the slat reveal a very interesting development.

The predicted pressure coefficient (C_p) distributions from CFD solutions over the slat for $\alpha = 19$–24 deg are plotted in Fig. 7. Because the flow around the LE is mainly along the y direction, this pressure distribution plot is displayed as y vs C_p; this y coordinate is not to be confused with the y/c corresponding to the surface normal direction. It can be seen in Fig. 7 that the suction peak is very close to the slat LE, and the suction C_p decreases with increasing angle of attack. Near maximum lift, the value of the pressure coefficient is approximately −25. This suggests that the flow around the slat LE has reached the compressibility limit, namely, the 0.7 vacuum value,[3] or $C_p M_{\text{fs}}^2 = -1$, where $M_{\text{fs}} = 0.2$. That is, the flow can no longer accelerate around the LE, and it reaches a maximum local Mach number around 1.5, which is also predicted by CFD as seen

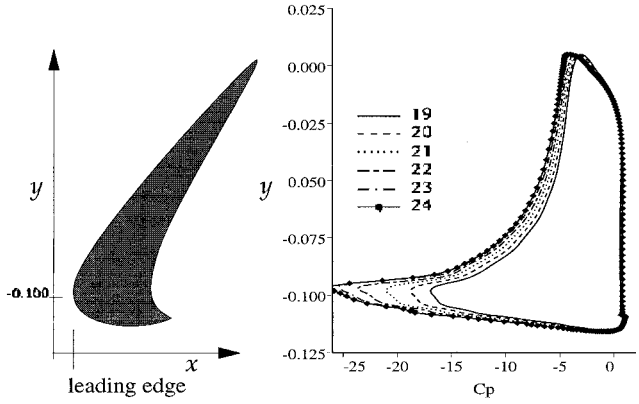

Fig. 7 Pressure coefficient over the slat for α = 19–24 deg.

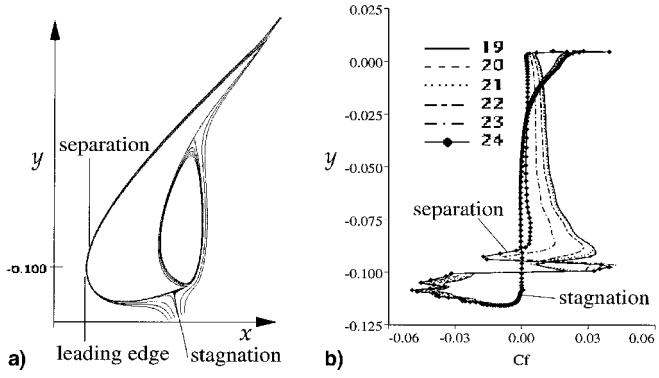

Fig. 8 a) Streamlines around the slat for α = 19 deg and b) skin friction coefficient over the slat for α = 19–24 deg.

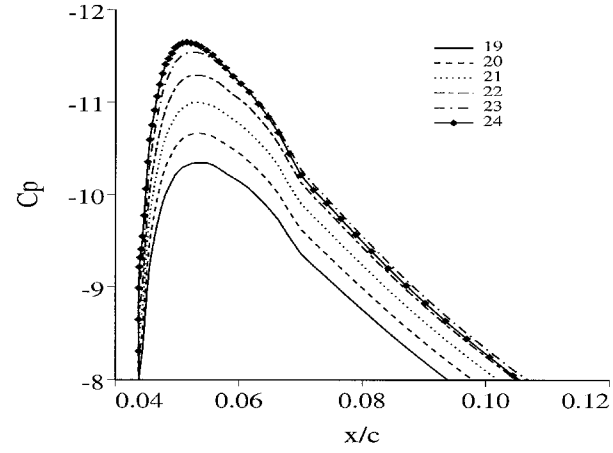

Fig. 9 Pressure coefficient distribution around the suction peak over the main element.

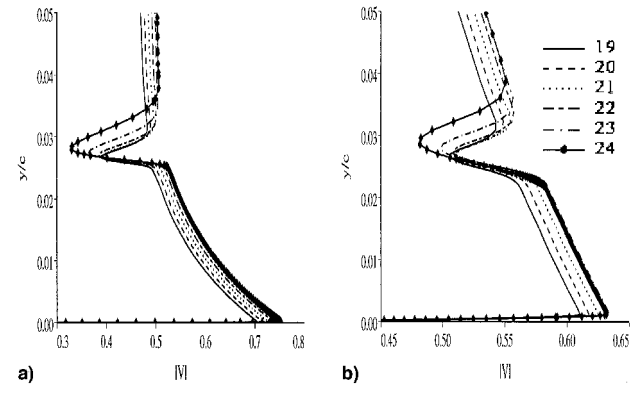

Fig. 10 Velocity profiles at suction peak and aft of suction peak. *x/c* = a) 0.05 and b) 0.10.

in Table 1. The location of this maximum Mach number is near the slat LE for every case.

Figures 8a and 8b show the predicted streamlines and skin friction coefficient (C_f) around the slat LE. The streamlines and stagnation point correspond to the solution at $\alpha = 19$ deg. For flow at higher angle of attack ($\alpha = 20$–24 deg), the stagnation point is located downstream closer to the cusp. From the stagnation point to the LE of the slat, the skin friction coefficient is negative because the flow is traveling upstream, not because of flow separation. Immediately downstream of the LE ($-0.1 < y < -0.075$), it can be seen that there are two distinctive groups of solutions. The solutions up to 21 deg exhibit similar features, namely, they show a trend toward separation as the local minimum C_f value approaches zero just aft the LE as α increases. In contrast, the solutions beyond 21 deg reach a much higher suction-peak skin friction value. This indicates that the flow just behind the LE is laminar below 21 deg, and turbulent above that. The flow around the slat LE also must slow down and separate at some point above 21 deg, because it has reached the compressibility limit as seen earlier. It is conceivable that for the experiment there is a separation bubble at the slat LE for $\alpha = 22$ deg, and the actual transition process itself prevents the bubble from becoming a huge LE (laminar) separation. Because the transition process is not modeled correctly, the CFD solution stays attached at $\alpha = 22$ deg. However, even with attached flow at the LE, the turbulent BL still separates at $\alpha = 23$ and 24 deg. Numerical experiments were performed to see if the fully turbulent flow assumption would yield the same results. As expected, for the CFD solutions with fully turbulent flow assumption, the maximum lift also occurs when the slat boundary separates and the C_p reaches the compressibility limit. The angle of attack for maximum lift is 24 deg, or 1 deg later than predicted with a transition assumption. The remaining question is: why should the slat separation prevent the main element from gaining more lift?

The main-element C_p distribution around the suction peak is plotted in Fig. 9 for $\alpha = 19$–24 deg. In general, the C_p around the suction peak becomes more negative as α increases; except at $\alpha = 24$ deg, this trend reverses downstream of the suction peak. This phenomenon on the surface is directly related to the slat wake. It can be seen in the velocity profiles at $x/c = 0.05$ and 0.10 (Figs. 10a and 10b, respectively) that the wake deficit growth is much larger above 22 deg. The flows with larger wake deficit must work harder to penetrate the adverse pressure-gradient region downstream of the main-element suction peak. Additionally, the displacement of the slat wake deficit and the near-surface flow in the confluent BL must satisfy the momentum conservation. This suggests that at stall, the reverse trend of the surface pressure downstream of the suction peak is coupled with the reduction of near-surface momentum. A near-surface enlarged velocity profile comparison before and after the suction peak confirms this hypothesis (Figs. 11a and 11b). Whether this is the true physical process of stall remains to be seen.

B. Trends: CFD Predictions vs Measurements

As reviewed in Sec. II, the effect of varying freestream Reynolds number has been shown to be similar to that of varying flap gap size. In particular, Woodward et al.[31] has demonstrated that, with increasing Reynolds number, the BLs and wakes reduce in thickness, and hence, the resulting behavior is strikingly similar to that achieved by increasing the flap gap at constant Reynolds number. In this work, we examine the trends caused by varying Reynolds number and flap gap by considering perturbations to a baseline airfoil and flow conditions, with the aim of better understanding the change in physics and shortcomings of CFD models. This trend study represents only a small subset of the entire scale effect investigation. Nonetheless,

the usefulness of CFD in the design of high-lift configurations depends to a large extent on the ability of CFD to predict correct lift increment trends and magnitudes corresponding to small changes, either in onset flow conditions or in the airfoil geometry.

1. Reynolds Number Effect

When the freestream Reynolds number is increased from $5M$ to $9M$, the measured lift increases by 0.078, or 1.9%, and the predicted lift (with transition locations specified) increases by 0.075, or 1.7%. The experimental repeatability in lift measurement is less than 1% at this flow condition (Mach 0.2, $\alpha = 19$ deg). CFD not only predicts a similar trend to that observed in the experiment, but also yields very good agreement in the magnitude of lift increase. The trend in the CBL development is also captured by the CFD simulation. The predicted and measured velocity profiles at locations 4–6, corresponding to the LE, midchord, and TE over the flap, are plotted in Figs. 12a (i)–(iii) and 12b (i)–(iii), respectively. It can be seen that the increase in Reynolds number results in a translation of the CBL profile down toward the flap surface. This means a reduction of the CBL displacement thickness as Reynolds number is increased from $5M$ to $9M$; this trend is consistent with the increase in lift.

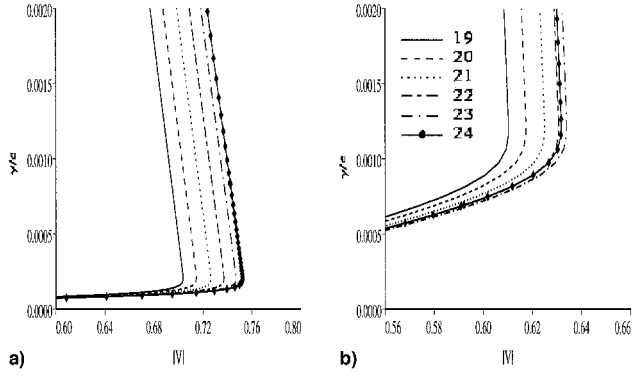

Fig. 11 Near-surface velocity profiles. x/c = a) 0.05 and b) 0.10.

2. Flap Gap Effect

Two configurations of the same airfoil with different flap gaps are studied for freestream conditions Mach = 0.2, $\alpha = 19$ deg, and $Re = 9M$. The baseline configuration has a flap gap of 1.27% chord, and is referred to as 30P30N. The other configuration has a gap size 1.5% chord, or 0.23% chord larger than the baseline flap gap size. This configuration is referred to as 30P30AD. It is observed[5] that the lift coefficient (C_L) increases by 0.043, or 1.00% that of the baseline configuration as the flap gap size is increased. In a separate tunnel entry, the lift increased by 0.94% for the same increase in gap size. The experimental data from the two tests are given in Table 2.

The lift coefficients from three sets of CFD solutions and $\%\Delta C_L$ because of increasing gap size are presented in Table 3, where FA

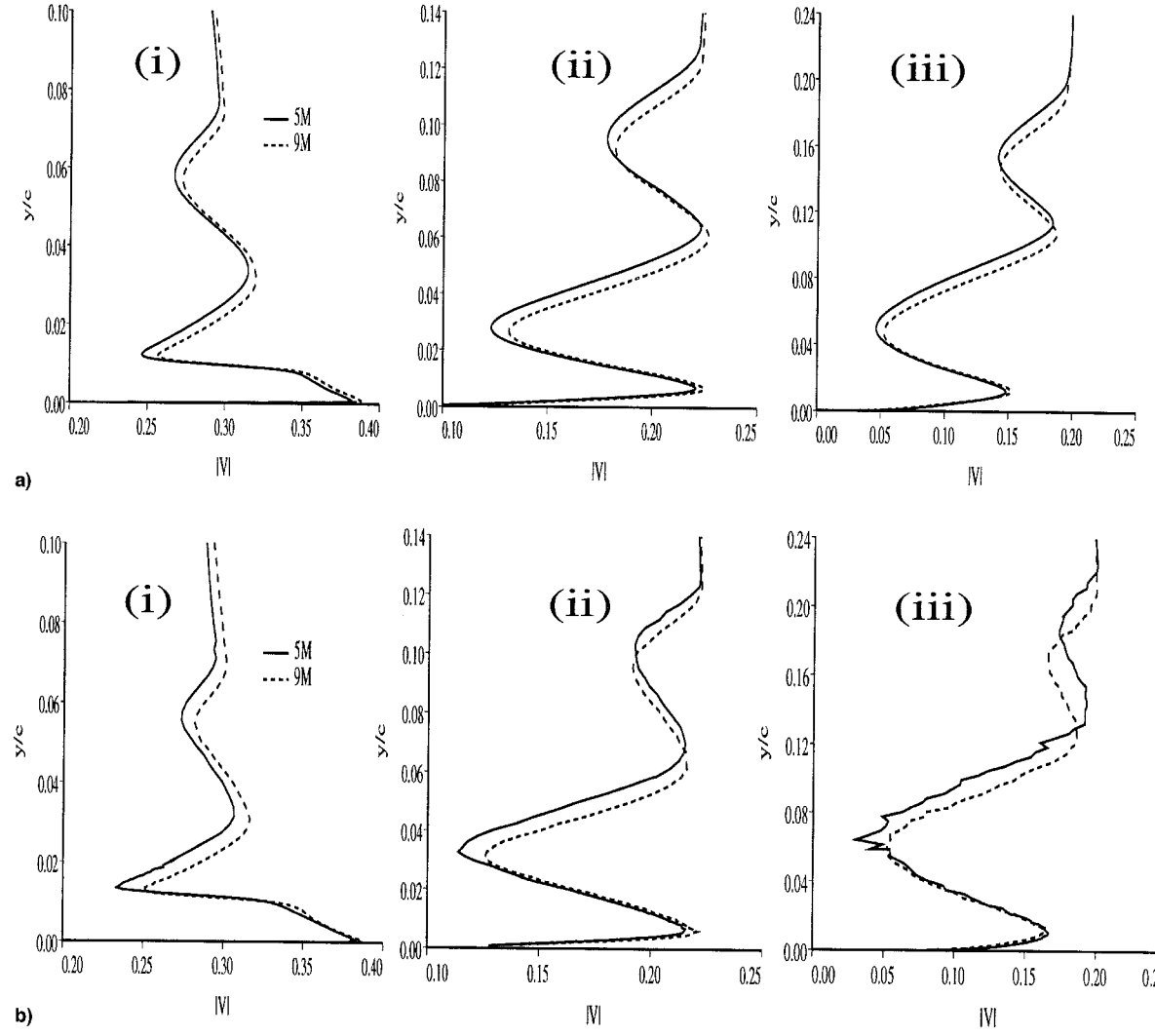

Fig. 12 Trend as a result of increasing Reynolds number. (i)–(iii) correspond to velocity profile locations 4–6: a) CFD predictions and b) experimental surveys.

Table 2 Measured lift coefficients and $\%\Delta C_L$ comparison

Test	Element	30P30N	30P30AD	% Delta
T1	Slat	0.7473	0.7591	0.275
	Main	3.1805	3.1993	0.439
	Flap	0.3563	0.3684	0.282
	Total	4.2841	4.3268	0.997
T2	Slat	0.7639	0.7697	0.133
	Main	3.2251	3.2474	0.513
	Flap	0.3554	0.3682	0.295
	Total	4.3444	4.3853	0.941

Table 3 CFD lift coefficients and $\%\Delta C_L$ comparison

CFD	30P30N	30P30AD	% Delta
FA1	4.4315	4.4446	0.296
FA2	4.4315	4.4941	1.413
WT	4.4542	4.5325	1.758

in the first column denotes the free-air boundary condition and grid assumption, and WT denotes the wind-tunnel walls boundary condition and grids. For the solutions in FA1, transition locations for the two configurations were assumed to be the same. For solutions in FA2 and WT, transition locations from the two configurations differ by 0.5%c over the main-element upper surface, and 0.2%c over the flap upper surface. This difference reflects the actual transition locations seen in the experiment.[43] The general trend of an increase in lift is predicted in all CFD solutions. The solutions from FA1 yield the least percentage increase. The individual element lift contributions indicate that the only increase in lift for the FA1 solutions is due to the flap. In contrast, both the FA2 and WT solutions show the largest increase in lift because of the main element, as seen in the experiment.

Two sets of predicted velocity profiles over the flap for these two configurations are plotted in Figs. 13a and 13b, which correspond to cases FA1 and WT, respectively. The profiles from FA2 are not shown here, but their trends are identical to those predicted by WT. The measured velocity profile surveys for the same locations and configurations are plotted in Fig. 13c. At the flap leading edge, the trend is the same between CFD and experiment, namely, a shift of the whole profile away from the surface as gap size is increased. This is expected, because the larger flap gap means a translation downward in the vertical distance of the flap surface with respect to the MTE, if the overhang (horizontal distance from the MTE) stays the same. However, downstream of this, the measured wakes show an apparent increased turning toward the surface for the increased gap size. This same trend is seen for the WT (Fig. 13b) as well as the FA2 solutions, but not for the solutions from FA1 (represented in Fig. 13a), in which transition location is identical for the two configurations. However, even the FA2 and WT cases do not show as much difference in wake position as the experiment.

The increase in flap gap size is on the order of the BL thickness. By widening the gap, it is similar to having a higher Reynolds-number flow through the gap. Therefore, it is not too surprising that the net effect observed when increasing the gap size is similar to that of increasing the freestream Reynolds number. That is, a reduction of overall displacement thickness at the flap trailing edge, and consequently, an increase in lift. In examining the measured trend (Fig. 13c), it is seen that there is a translation for the layer adjacent to the flap wall up to the main-element wake centerline (y/c between 0 and 0.06) over the whole flap surface. This translation is predicted by all CFD solutions, suggesting that for the wall layer and inner half-wake caused by the main element, CFD does a fairly good job of predicting the trend caused by the gap change. However, it remains an open question as to whether the disagreement between CFD and experiment outside this inner layer is a result of further transition location differences between configurations not yet accounted for, or whether CFD is unable to model an actual increased wake turning rate for the larger flap gap case.

While the predicted trends due to the CBL development are not quite the same, all CFD predictions show an increase in lift with increasing flap gap size. It is not clear what the impact of different CBL trends is on the total circulation. However, from the FA1 solutions it is apparent that CFD only predicted the increased circulation over the flap if the slat and main element transition remains the same. Whether the increase of circulation over the main element and slat is because of differences of transition location or wake modeling, or a combination of these factors, the results definitely suggest that the solution requires correct coupling of inviscid and viscous physics. Furthermore, the merging and turning effects of the wakes require that all aspects of the physics be modeled appropriately, including transition and turbulence, and possibly unsteady phenomena that we have not begun to understand.

C. Wakes: Merging and Turning

As seen in previous sections, wake prediction is crucial to the accuracy and convergence of the overall CFD solution. Here we examine in detail why the CFD predicted wakes may have different merging or turning rates from those observed in experiment. We have tried grid adaption by aligning the wake grids to streamlines, local grid refinement at the MTE, application of the thin-layer assumption in both wall-normal and streamwise directions, and full-RANS simulations. None of these produced any significant changes in the rates of merging and turning of the wakes.

In investigating the wakes of the CBL, it is desirable to study the slat flow first, because its effect is convected all the way downstream. However, the flow scale at the slat and main-element leading edge, e.g., location 1 in Fig. 4, is so small that the accuracy of measurements for an intrusive experimental survey is affected by spatial resolution as well as some unsteadiness in the flow emerging from the slat cove.[33] As seen in the profile of the slat wake in Fig. 6, it is possible that the earlier merging in the measured profile is due to flow from the slat cove. It is also likely that uncertainties in slat transition play a key role in differences between the CFD and measured slat wake width and depth.[7] This unsteady phenomenon and slat transition effects are beyond the scope of the current work; therefore, we will focus instead on the wake from the main element and its development over the flap.

1. *Flow at MTE*

Figures 14a and 14b show velocity profiles and the corresponding Reynolds stress profile comparisons at the MTE (location 3). The agreement between CFD and experiment is excellent in the wall layer ($y/c \sim 0$–0.02), but the prediction of the slat wake and merging region is poor. Additionally, the predicted Reynolds stress still shows a small region of potential core ($y/c \sim 0.02$), indicating that the slat wake has not yet merged in the CFD solution. These differences are likely linked to the difficulties of modeling the transition and possible unsteady flow originating with the slat, as mentioned earlier. The layer adjacent to the wall shows generally good agreement between predicted and measured stresses, with only a relatively small difference in the maximum stress level, which may be attributed to the probe and wall interference in the experiment. Based on the generally good agreement between CFD and experiment in the main-element BL, it is observed that the Boussinesq eddy viscosity hypothesis is valid at this location.

The velocity profile on the flap leading edge, immediately downstream of the MTE at 89.8%c (location 3), is plotted in Fig. 15a. It should be noted that the y axis is shifted by $\sim 0.01c$ below the surface, such that $y/c = 0$ corresponds to the MTE. Features of this profile are similar to those exhibited by the profiles at 85%c, although there are some differences in the slope of the outer-half-wake profile and the maximum wake deficit due to the main element between CFD and experiment. The corresponding Reynolds stress comparison (Fig. 15b) reveals that the CFD underpredicts the measured

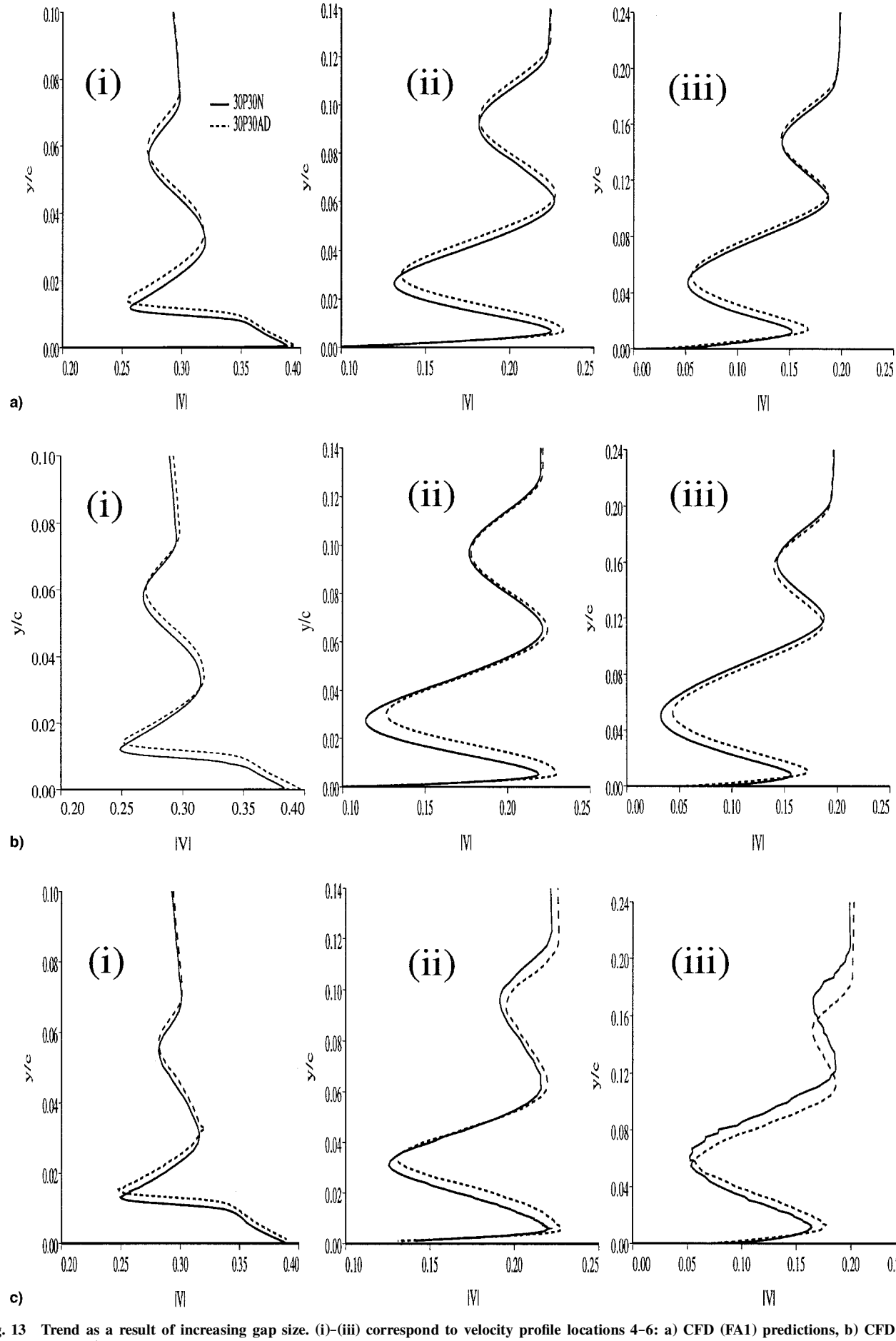

Fig. 13 Trend as a result of increasing gap size. (i)–(iii) correspond to velocity profile locations 4–6: a) CFD (FA1) predictions, b) CFD (WT) predictions, and c) experimental surveys.

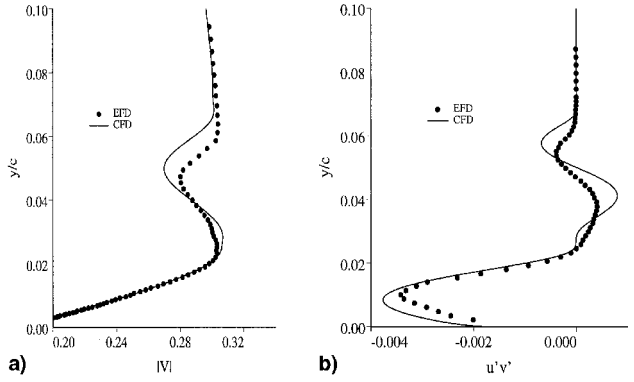

Fig. 14 a) Velocity profile comparison at $x/c = 0.85$ and b) Reynolds shear-stress comparison.

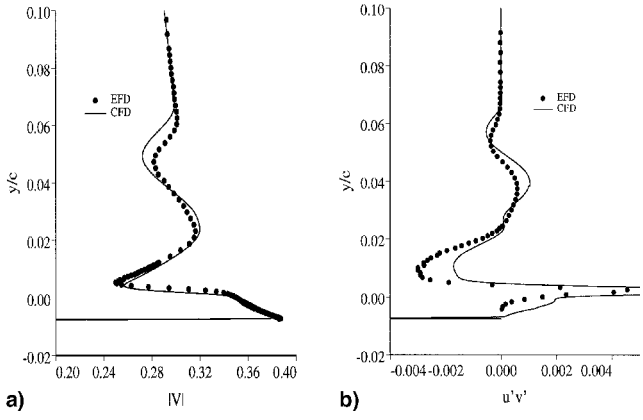

Fig. 15 a) Velocity profile comparison at $x/c = 0.898$ and b) Reynolds shear-stress comparison.

levels for the main-element wake. It is curious that, even though the two stations represented in Figs. 14 and 15 are only 5%c apart, the predictions are markedly different. A rotation of the Reynolds stresses to different coordinates does not change the comparison outcome here, because the flow is still mostly parallel to the surface at this location.

Figure 16a displays the measured Reynolds stress profiles at locations 3 and 4. It can be seen that there is very little difference between the two curves. The parts corresponding to the inner half wakes show more difference than other parts. In contrast, the comparison of the predicted stresses shows large differences in the main-element wake (see Fig. 16b); the predicted $u'v'$ maximum magnitude (at 89.8%c) is less than half of that due to the wall layer (at 85%c) for $y/c \sim 0.01$. To see how this large discrepancy develops between the CFD profiles at the MTE and the flap LE, we investigate the flowfield solution and examine each relevant variable leading to the peculiar behavior of the Reynolds stresses.

Predicted contours of Reynolds shear stress ($u'v'$) rotated to the local streamline direction at each point are presented in Fig. 17. The corresponding strain-rate (S_{12}) and eddy viscosity (μ_t) contours are shown in Fig. 18 and Fig. 19, respectively. In Fig. 17, the multiple shear layers having positive and negative shear-stress values (observed in Figs. 13–15) are seen as contour lines parallel to airfoil surfaces. In particular, it is interesting to note that the negative contours closest to the surfaces (between y/c of 0 and 0.02) do not continue downstream smoothly over the MTE. There is a local minimum in $u'v'$ over the MTE. This explains why we see an increase in predicted $u'v'$ at the flap leading edge ($x/c = 0.898$) between y/c of 0 and 0.02 compared with that at the MTE (Figs. 14–16).

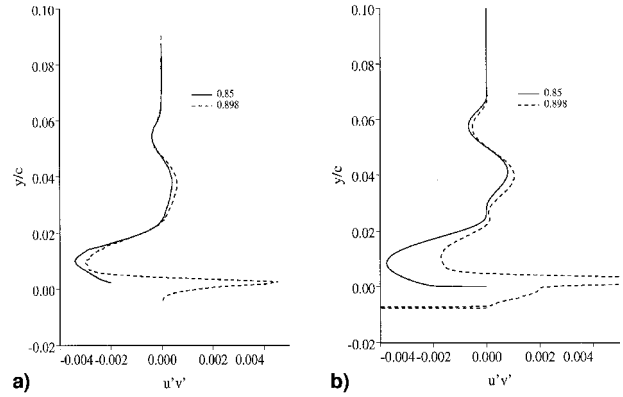

Fig. 16 a) Experimental Reynolds stress comparison and b) CFD Reynolds stress comparison.

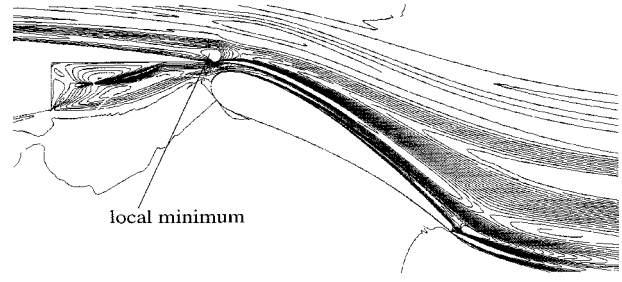

Fig. 17 Reynolds shear-stress ($u'v'$) contours.

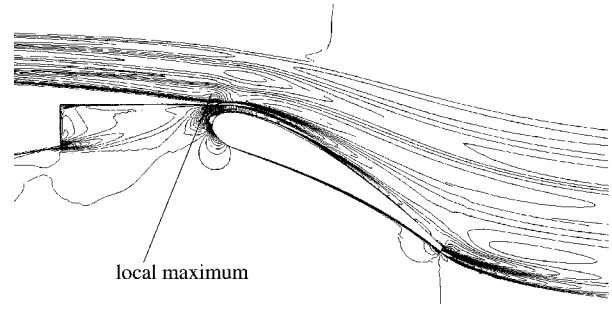

Fig. 18 Strain-rate (S_{12}) contours.

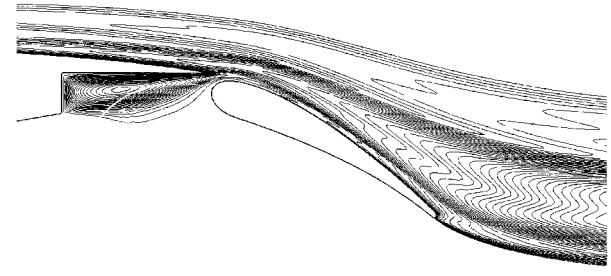

Fig. 19 Eddy viscosity (μ_t) contours.

The strain-rate contours (Fig. 18) exhibit a similar behavior as the predicted Reynolds stress contours, except there is a local maximum over the MTE in the same shear layer. On the contrary, the eddy viscosity contour levels (Fig. 19) vary smoothly in the streamwise direction around the MTE. This shows how simplistic eddy viscosity is. The simple formula relating Reynolds shear stress and strain rate is as follows:

$$-u'v' = \mu_t S_{12} \tag{2}$$

Bradshaw[¶] has stated that

> Eddy viscosity is the ratio of a Reynolds stress to a mean strain rate (note that this is a *definition* involving quantities that can be measured, not a *hypothesis*). Reynolds stresses and mean strain rates develop in different ways—for example, pressure gradients affect mean strain rates but do not directly affect Reynolds stresses—so that the *hypothesis* that eddy viscosity is isotropic and well-behaved is not reliable.

In the real flow (Fig. 16a), the Reynolds stress barely reacts to the mean-flow gradient at the MTE in the short distance of 5% chord. In other words, there is a "lag" in the development of the Reynolds stresses with respect to changes in the mean flow. This is seen as the strain rate S_{12} varies rapidly in the vicinity of the MTE, where the flow is suddenly free to turn, and immediately downstream at the flap LE it is also subjected to considerable pressure gradient. Naturally, using the strain rate scaled by a simple constant for predicting the Reynolds stress leads to the nonphysical behavior seen in the CFD solution.

2. *Flow over Flap at Midchord*

Because the predicted Reynolds stress in the main-element wake is deficient at the flap LE, we can hold no expectation for agreement between CFD and experiment downstream over the flap. Nevertheless, we now turn our attention to the midflap location to demonstrate a potential pitfall of isotropic eddy viscosity models in this region. The velocity and Reynolds stress profiles at the flap midchord location $x/c = 1.032$ are plotted in Figs. 20a and 20b. As expected, neither the predicted slat wake nor main-element wake are in good agreement with the experiment. However, the corresponding Reynolds stress comparison reveals a very interesting feature. The solid symbols and curve in Fig. 20b correspond to Reynolds stresses evaluated in local BL coordinates, and the open circles and dashed curve are $u'v'$ rotated to local SL coordinates using Eq. (1). It can be seen that the profiles from experiment and CFD are quite different in the region of the main-element wake. In particular, the CFD predictions in both BL and SL coordinates show a clear distinction of positive and negative regions corresponding to the negative and positive slopes of the velocity profile, following the Boussinesq eddy viscosity approximation. The measured Reynolds stresses in flap BL coordinates, however, have no negative part at all, except for the region very close to the surface. The measured stresses in local SL coordinates do show the expected negative and positive regions, though the difference from CFD prediction remains large.

Some insight into the reason for the difference between CFD and measurement in the region where $u'v' < 0$ can be gained by looking for the coordinate orientation that maximizes the Reynolds shear stress. The angle for maximum shear (MS) stress can be written as

$$\theta = \tfrac{1}{2}\tan^{-1}\left[\tfrac{1}{2}(v'v' - u'u')\Big/u'v'\right] \tag{3}$$

A plot of the maximum Reynolds shear-stress comparison is given in Fig. 21a, where the symbols represent data after rotation to the maximum shear-stress coordinates. It is seen that agreement of the negative parts of the Reynolds shear stress between CFD and experiment is much better in MS coordinates than in BL or SL coordinates (see Fig. 20b). Because the eddy viscosity implied by Eq. (2) is a scalar, independent of direction, the Reynolds stress tensor and the strain-rate tensor in CFD are aligned. Consequently, the direction of MS stress (θ) equals the direction of the MS strain rate (ϕ), which can be obtained in a form similar to Eq. (3), as

$$\phi = \tfrac{1}{2}\tan^{-1}\left[\tfrac{1}{2}(S_{22} - S_{11})\Big/S_{12}\right] \tag{4}$$

Another way to interpret the preceding equation is that "The models are designed to predict the *strainwise* component of stress," as illustrated by Driver.[44] For most simple BL-type flows, the maximum strain-rate direction is almost aligned with the streamwise direction; thus most eddy viscosity models are calibrated to give accurate prediction of the streamwise component of shear stress.

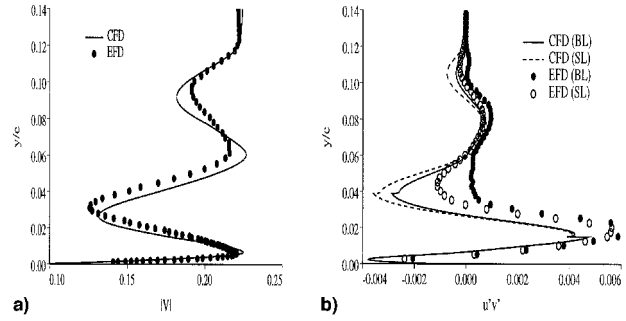

Fig. 20 a) Velocity profile at $x/c = 1.032$ and b) Reynolds stress profile at $x/c = 1.032$.

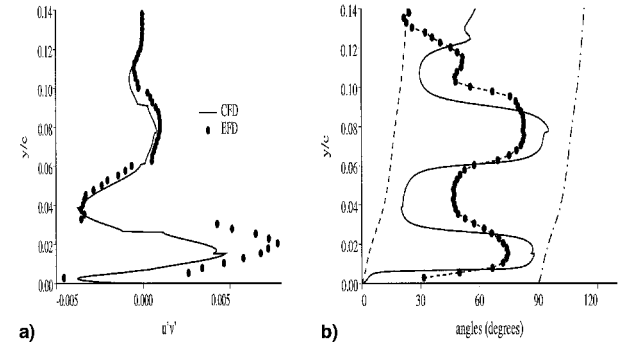

Fig. 21 a) Maximum Reynolds stress profile at $x/c = 1.032$ and b) CFD maximum strain-rate angle ϕ (solid) vs experimental MS stress angle θ (symbols): – – –, SL angle, and –·–·–, SL angle +90 deg.

For the high-lift flow case with multiple shear layers merging and turning, and producing a very complex and thick CBL, not only is the MS strain-rate direction not aligned with the streamwise direction, but also the direction changes back and forth from the surface to the edge of the CBL. This can be seen in Fig. 21b, where both experimental MS stress angle (symbols) and CFD maximum strain-rate angle (solid line) increase and decrease several times in the CBL. In the same figure, the dashed line depicts the SL angle, and the dash–dot line depicts the SL angle plus 90 deg (note that this represents the angle of the orthogonal eigenvector). All of these angles are taken with respect to the surface at $x/c = 1.0321$. It can be seen that, for the CFD maximum strain-rate angle, the BL resulting from the flap and the outer half-wakes due to the main element ($0.03 < y/c < 0.06$) and slat ($0.09 < y/c < 0.12$) have directions within 30 deg to the SL angle, whereas the inner half-wakes are within 30 deg to the orthogonal eigenvector direction, or are within −30 deg to the SL angle itself. This is expected because the shear changes sign through these wakes, resulting in the eigenvectors of S_{ij} switching to different directions. Hence, although the maximum strain-rate angle is within 30 deg of the SL angle in most areas, the eddy viscosity model may have an adverse impact in narrow regions where the maximum stress angle is far from the SL angle. Moreover, these narrow regions are also where the stress and production are the highest. Another observation from Fig. 21b is that the experimental MS stress angle is not as symmetric as the CFD maximum strain-rate angle. Namely, the angles corresponding to the inner-half wakes are closer to the SL angle plus 90 deg than those angles in the outer half-wakes are to the SL angles. In particular, it is seen that the experimental MS stress angle is almost 45 deg away from the two SL angles between y/c of 0.03 and 0.06. Overall, it can also be seen that the experimental and CFD angles do not always switch directions at the same y/c. The comparisons in Fig. 21b suggest that the poor agreement we have for the Reynolds stresses is in part a result of the inherent inability of the isotropic eddy viscosity model to predict the same magnitude and direction (relevant to the transport of momentum) of the Reynolds stresses.

[¶]Bradshaw, private communication, Stanford Univ., Stanford, CA, 1998.

V. Conclusions

The analysis of representative cases investigated, in light of the knowledge gained from the numerical and experimental data, suggests the following conclusions:

1) Global convergence of high-lift flows is inhibited by particularly slow convergence of the wakes. Research to uncover the root cause of this wake convergence problem is essential, particularly for CFD in three-dimensional high-lift design applications.

2) At maximum lift, flow unsteadiness is observed in the experiment. The RANS simulation at the same angle of attack does not show unsteadiness. However, instability in numerics is observed if a non-time-accurate approach is taken to converge the solution.

3) The maximum lift predicted by CFD occurs when flow over the slat reaches the compressibility limit. At the predicted maximum lift, although there is no separation over the flap, the slat boundary layer separates, resulting in a thickened slat wake, which, in turn, causes the main element to stall because of momentum displacement. Whether this is the physical phenomenon that limits maximum lift remains to be seen.

4) Based on the comparison of the lift increase and the changes in velocity profile development in the CBLs between CFD and measured data, we conclude that the trend caused by increasing Reynolds number from $5M$ to $9M$ is predicted by CFD, and the trend caused by increasing flap gap size by 0.23% chord is not clearly captured by CFD. The success in the Reynolds number trend prediction indicates that CFD can capture the translational effect in the CBLs. Nonetheless, the merging and turning effects require that all aspects of the physics be modeled appropriately, including transition and turbulence, and possibly unsteady phenomena that are not addressed in this study.

5) Eddy viscosity is not reliable for predicting the physics of wake confluence in high-lift flows. It is demonstrated that, because of the CFD-predicted Reynolds stresses reacting instantaneously to the shear-strain rates, the results of wake confluence (at MTE) disagree with those seen in the experiment.

6) Predicted Reynolds shear-stress profiles at the midflap location do not agree with measured data, particularly in the outer-half wake from the main element. Part of the discrepancy is a result of poor upstream prediction of the Reynolds stresses; however, there is also a question regarding the coordinate system in which it is appropriate to compare the actual Reynolds shear-stress and CFD results using eddy viscosity models. Nevertheless, considering the oscillatory character of the maximum strain-rate angle as well as the disparity between the measured MS stress angles and the computed maximum strain-rate angles at the midflap location, it is evident that the isotropic eddy viscosity assumption is not strictly valid and may even be damaging for predicting the physics of CBLs in this region of the high-lift flowfield.

The focus of this paper is to determine the degree to which viscous flow physics is correctly represented by CFD. However, the complexity of the physics (including flow unsteadiness, uncertainties in transition locations, and strong inviscid–viscous couplings) and limitations of the experiment (such as tunnel wall effects and three dimensionality at maximum lift) make it difficult to draw general conclusions. It is therefore unclear how much the poor predictions of engineering quantities, such as lift trend, are a result of poor modeling of turbulence, and how much are a result of other factors. Research attempting to isolate and quantify the impact of predicted viscous properties on the overall high-lift solution accuracy is clearly warranted.

Acknowledgments

The authors thank John B. Anders, Peter Bradshaw, Kuo-Cheng Chang, David Driver, Thomas Gatski, Antony Jameson, Dennis Johnson, Abdi Khodadoust, and most of all, Philippe Spalart, for their helpful discussions.

References

[1]Smith, A. M. O., "Wing Design and Analysis—Your Job," *2nd Symposium on Numerical and Physical Aspects of Aerodynamics Flows*, California State Long Beach Univ., CA, 1983.

[2]Nield, B. N., "An Overview of the 777 High Lift Aerodynamic Design," *Proceedings of the High Lift and Separation Control Conference*, Royal Aeronautical Society, Bath, England, UK, 1995, pp. 1.11–1.14.

[3]Smith, A. M. O., "High-Lift Aerodynamics," *Journal of Aircraft*, Vol. 12, No. 6, 1975, pp. 501–530.

[4]Jameson, A., "Re-Engineering the Design Process Through Computation," AIAA Paper 97-0641, Jan. 1997.

[5]Lynch, F. T., Potter, R. C., and Spaid, F. W., "Requirements for Effective High Lift CFD," *International Council of the Aeronautical Sciences Proceedings, 20th Congress*, AIAA, Reston, VA, 1996.

[6]Bucci, G. S., and Sullivan, J. P., "An Experimental Simulation of High Lift Wake Flows at High Reynolds Number," AIAA Paper 97-2297, June 1997.

[7]Rumsey, C. L., Gatski, T. B., Ying, S. X., and Bertelrud, A., "Prediction of High-Lift Flows Using Turbulent Closure Models," *AIAA Journal*, Vol. 36, No. 5, 1998, pp. 765–774.

[8]Johnston, L. J., and Horton, H. P., "An Experimental Study of Turbulent Wake/Boundary Layer Mixing Flows," AIAA/International Council of the Aeronautical Sciences, TR 86-2.3.4, Reston, VA, Sept. 1986.

[9]Seetharam, H. C., and Wentz, W. H., "A Low Speed Two-Dimensional Study of Flow Separation on the GA(W)-1 Airfoil with 30% Chord Fowler Flap," NASA CR-2844, 1977.

[10]Braden, J. A., Whipkey, R. R., Lilley, D. E., Jones, G. S., and Morgan, H. L., "Application of Laser Velocimetry to the Study of the Flow Around a Two-Dimensional Airfoil," AIAA Paper 86-505, Jan. 1986.

[11]Obert, E., "Forty Years of High-Lift R&D—An Aircraft Manufacturer's Experience," *High Lift System Aerodynamics*, CP-515, AGARD, Sept. 1993.

[12]Cornish, J. J., III., "Practical High Lift Systems Using Distributed Boundary Layer Control," Aerophysics Dept., Mississippi State Univ. Research Rept. 19, Dec. 1958.

[13]Petrov, A. V., "Certain Types of Separated Flow over Slotted Wings," *Fluid Mechanics—Soviet Research*, Vol. 7, No. 5, 1978, pp. 80–89.

[14]Nakayama, A., Kreplin, J. P., and Morgan, H. L., "Experimental Investigation of Flowfield About a Multi-Element Airfoil," *AIAA Journal*, Vol. 28, No. 1, 1990, pp. 14–21.

[15]Valarezo, W. O., "High Lift Testing at High Reynolds Numbers," AIAA Paper 92-3986, July 1992.

[16]Spaid, F., and Lynch, F., "High Reynolds Number, Multi-Element Airfoil Flowfield Measurements," AIAA Paper 96-0682, Jan. 1996.

[17]Chin, V., Peters, D., Spaid, F., and McGhee, R., "Flowfield Measurements About a Multi-Element Airfoil at High Reynolds Numbers," AIAA Paper 93-3137, July 1993.

[18]Brune, G. W., and Sikavi, D. A., "Experimental Investigation of the Confluent Boundary Layer of a Multielement Low Speed Airfoil," AIAA Paper 83-0566, Jan. 1983.

[19]Bario, F., Charnay, G., and Papailiou, K. D., "An Experiment Concerning the Confluence of a Wake and a Boundary Layer," *Journal of Fluids Engineering*, Vol. 104, March 1982, pp. 18–24.

[20]Zhou, M. D., and Squire, L. C., "The Interaction of a Wake with a Turbulent Boundary Layer," *Aeronautical Journal*, Vol. 89, 1985, pp. 72–81.

[21]Agoropoulos, D., and Squire, L. C., "Interactions Between Turbulent Wakes and Boundary Layers," *AIAA Journal*, Vol 26, No. 10, 1988, pp. 1194–1200.

[22]Squire, L. C., "Interactions Between Turbulent Wakes and Boundary Layers," *Progress in Aerospace Sciences*, Vol. 26, 1989, pp. 261–288.

[23]Fejtek, I., "Summary of Code Validation Results for a Multiple Element Airfoil Test Case," AIAA Paper 97-1932, July 1997.

[24]Hinze, J. O., "Turbulent Flow Regions with Shear Stress and Mean Velocity Gradient of Opposite Sign," *Applied Scientific Research Journal*, Vol. 22, No. 3/4, 1970, pp. 163–317.

[25]Mathieu, J., "Remarks on Turbulent Flows with Free Stream Boundaries," von Kármán Inst., Rept. VKI-LS-36, Rhode-Saint-Genese, Belgium, April 1971.

[26]Johnson, D. A., Menter, F. R., and Rumsey, C. L., "The Status of Turbulence Modeling for External Aerodynamics," AIAA Paper 94-2226, June 1994.

[27]Haines, A. B., "Scale Effects on Aircraft and Weapon Aerodynamics," AGARD, AG-323, July 1994.

[28]Haines, A. B., "Scale Effects on $C_{L_{\max}}$ at High Reynolds Number," *Proceedings of High Lift and Separation Control Conference*, Royal Aeronautical Society, Bath, England, UK, 1995, pp. 28.1–28.14.

[29]Mack, M. D., and McMasters, J. H., "High Reynolds Number Testing in Support of Transport Airplane Development," AIAA Paper 92-3982, July 1992.

[30]Valarezo, W. O., "Topics in High-Lift Aerodynamics," AIAA Paper 93-3136, July 1993.

[31]Woodward, D. S., Hardy, B. C., and Ashill, P. R., "Some Types of Scale Effect in Low-Speed High-Lift Flows," International Council of the Aeronautical Sciences, Paper 88-4.9.3, Sept. 1988.

[32]Lueptow, R. M., Breuer, K. S., and Haritonidis, J. H., "Computer-Aided Calibration of X-Probes Using a Look-Up Table," *Experiments in Fluids*, Vol. 6, 1988, pp. 115–118.

[33]McGinley, C. B., Anders, J. B., and Spaid, F. W., "Measurements of Reynolds Stress Profiles on a High-Lift Airfoil," AIAA Paper 98-2620, June 1998.

[34]Vatsa, V. N., Thomas, J. L., and Wedan, B. W., "Navier–Stokes Computations of Prolate Spheroids at Angle of Attack," *Journal of Aircraft*, Vol. 26, No. 11, 1989, pp. 986–993.

[35]Thomas, J. L., Krist, S. L., and Anderson, W. K., "Navier–Stokes Computations of Vortical Flows over Low Aspect-Ratio Wings," *AIAA Journal*, Vol. 28, No. 2, 1990, pp. 205–212.

[36]Thomas, J. L., "Reynolds Number Effects on Supersonic Asymmetrical Flows over a Cone," *Journal of Aircraft*, Vol. 30, No. 4, 1993, pp. 488–495.

[37]Rumsey, C. L., Sanetrik, M. D., Biedron, R. T., Melson, N. D., and Parlette, E. B., "Efficiency and Accuracy of Time-Accurate Turbulent Navier–Stokes Computations," *Computers and Fluids*, Vol. 25, No. 2, 1996, pp. 217–236.

[38]Roe, P., "Approximate Riemann Solvers, Parameter Vectors, and Difference Schemes," *Journal of Computational Physics*, Vol. 43, No. 2, 1981, pp. 357–372.

[39]Jones, K. M., Biedron, R. T., and Whitlock, M., "Application of a Navier–Stokes Solver to the Analysis of Multielement Airfoils and Wings Using Multizonal Grid Techniques," AIAA Paper 95-1855, June 1995.

[40]Jasper, D. W., Agrawal, S., and Robinson, B. A., "Navier–Stokes Calculations on Multi-Element Airfoils Using a Chimera-Based Solver," CP-515, AGARD, Sept. 1993, pp. 8.1–8.11.

[41]Morrison, J. H., "Numerical Study of Turbulence Model Predictions for the MD 30P/30N and NHLP-2D Three-Element High-Lift Configurations," NASA/CR-1998-208967, Dec. 1998.

[42]Spalart, P., and Allmaras, S., "A One-Equation Turbulence Model for Aerodynamic Flows," *La Recherche Aerospatiale*, Vol. 1, 1994, pp. 5–21.

[43]Bertelrud, A., "Transition on a Three-Element High Lift Configuration at High Reynolds Numbers," AIAA Paper 98-0703, Jan. 1998.

[44]Driver, D. M., "Reynolds Shear Stress Measurement in a Separated Boundary Layer," AIAA Paper 91-1787, June 1991.